A convolutional neural network approach to estimate earthquake kinematic parameters from back-projection images

Corradini M. [1], McBrearty I.W. [2], Trugman D.T. [3], Satriano C. [4], Johnson P.A. [5], Bernard P. [4]

[1] European-Mediterranean Seismological Centre, France; [2] Stanford University, USA; [3] The University of Texas at Austin; [4] Université de Paris, Institut de physique du globe de Paris, France; [5] Los Alamos National Laboratory, USA.

Corresponding author:
Marina Corradini
E-mail: marina.corradini@emsc-csem.org
Tel: +33 769 31 75 00

Abbreviated title: Convolutional neural network for earthquake rupture parameter estimation

This manuscript has been submitted for publication in *Geophysical Journal International*. This is a Preprint and has not been peer reviewed yet.

Abstract

The retrieval of earthquake finite-fault kinematic parameters after the occurrence of an earthquake is a crucial task in observational seismology. Routinely-used source inversion techniques are challenged by limited data coverage and computational effort, and are subject to a variety of assumptions and constraints that restrict the range of possible solutions. Back-projection (BP) imaging techniques do not need prior knowledge of the rupture extent and propagation, and can track the high-frequency (HF) radiation emitted during the rupture process. While classic source inversion methods work at lower frequencies and return an image of the slip over the fault, the BP method underlines fault areas radiating HF seismic energy. HF radiation is attributed to the spatial and temporal complexity of the rupture process (e.g., slip heterogeneities, changes in rupture speed and in slip velocity). However, the quantitative link between the BP image of an earthquake and its rupture kinematics remains unclear. Our work aims at reducing the gap between the theoretical studies on the generation of HF radiation due to earthquake complexity and the observation of HF emissions in BP images. To do so, we proceed in two stages, in each case analyzing synthetic rupture scenarios where the rupture process is fully known. We first investigate the influence that spatial heterogeneities in slip and rupture velocity have on the rupture process and its radiated wave field using the BP technique. We simulate different rupture processes using a 1D line source model. For each rupture model, we calculate synthetic seismograms at three teleseismic arrays and apply the BP technique to identify the sources of HF radiation. This procedure allows us to compare the BP images with the causative rupture, and thus to interpret HF emissions in terms of along-fault variation of the three kinematic parameters controlling the synthetic model: rise time, final slip, rupture velocity. Our results show that the HF peaks retrieved from BP analysis are better associated with space-time heterogeneities of slip acceleration. We then build on these findings by testing whether one can retrieve the kinematic rupture parameters along the fault using information from the BP image alone. We apply a machine learning, convolutional neural network (CNN) approach to the BP images of a large set of simulated 1D rupture processes to assess the ability of the network to retrieve from the progression of HF emissions in space and time the kinematic parameters of the rupture. These rupture simulations include along-strike heterogeneities whose size is variable and within which the parameters of rise-time, final slip, and rupture velocity change from the surrounding rupture. We show that the CNN trained on 40,000 pairs of BP images and kinematic parameters returns excellent predictions of the rise time and the rupture velocity along the fault, as well as good predictions of the central location and length of the heterogeneous segment. Our results also show that the network is insensitive towards the final slip value, as expected from a theoretical standpoint.

Keywords: Computational seismology, Earthquake source observations, Neural networks, Numerical modelling

1. Introduction

Characterizing earthquake finite-fault parameters, such as the rupture extent, rupture velocity, and the spatio-temporal distribution of the slip along the fault, are all fundamental to achieving a better understanding of earthquake dynamics. Earthquake parameters are often estimated through slip inversion techniques that rely on a-priori assumptions on the fault geometry and the rupture mechanism. Such techniques have succeeded to image the finite-fault parameters in a relatively low-frequency range ($f < 2.0$ - 3.0 Hz) (e.g., Zeng et al. 1993; Mai et al, 2016). However, if we are interested in uncovering fine-scale, detailed structure in the rupture process, high-frequency (HF) waveform data must be taken into account (e.g. Mendoza and Hartzell 1988, Ide 1999).

The complexity of the source manifests itself in terms of short-period seismic waves, at frequencies higher than the corner frequency f_c (e.g. Madariaga 1977, Spudich and Frazer 1984, Ruiz et al. 2011) controlled by the source duration. At these higher frequencies, the classic inversion techniques are no longer adequate, both because of computational limitations and by our lack of knowledge of the Earth's structure at those frequencies. Hence, high-resolution imaging techniques, such as the back-projection (BP, Ishii et al. 2005), have recently become a prominent means to unraveling aspects of the rupture complementary to the ones supplied by classic inversion. When applied to teleseismic body-waves, the BP method takes advantage of the coherence of HF waveforms among traces recorded at nearby stations. This technique requires minor a priori constraints and bypasses the procedure of inverting for Earth structure (e.g., Kiser and Ishii 2017). BP has become a very popular method and several observational studies in recent years have highlighted the ability of such a technique to illuminate the HF emission sources excited during earthquake rupturing (e.g., Walker and Shearer 2009, Xu et al. 2009, Zhang and Ge 2010, Meng et al. 2011, Koper et al. 2011, Lay et al. 2012, Satriano et al. 2014, Vallée and Satriano 2014, Grandin et al. 2015). From a theoretical perspective, studies have long attributed the generation of HF radiation during earthquake faulting to small-scale variations or roughness in final slip, slip velocity, or rupture velocity —acceleration and deceleration— over the fault plane (Madariaga 1977, Andrews 1981, Herrero and Bernard 1994, Somerville et al. 1999, Ruiz et al. 2011). HF radiation enlightened by BP images of large earthquakes could, therefore, help constrain the variability of parameters controlling the rupture process. However, unanimous consent on how the BP image relates to earthquake parameters has not yet been achieved. Specifically, Ishii et al. (2005) suggested that the BP image of the earthquake is related to the radiated seismic energy. Both works from Yao et al. (2012) and Fukahata et al. (2014) point out an intrinsic ambiguity in BP image towards resolving slip velocity or slip acceleration.

Our work has, therefore, a dual purpose. First, we aim to investigate the link between coherent images of the rupture process and the mechanism of high-frequency (HF) generation and, therefore, our understanding of what the BP image truly represents. Second, we work toward extracting information on the earthquake kinematic properties from the HF radiation enhanced by the BP analysis of earthquakes. To accomplish the objectives of our study, we take a data-driven approach, where for a Mw 7.5 strike-slip event we simulated 40,000 rupture scenarios with different characterizing traits. We parameterize the system as a 1D line source model (Lancieri and Zollo 2009). This choice allows us to ease the computational effort and describe the complex earthquake rupture process in a simplified manner that seeks to represent its key elements by three kinematic parameters: the rise time, the final slip, and the rupture velocity. We apply the back-projection technique and compare the resulting images with the originating rupture model. Doing so enables us to understand not only the link between the generation of HF radiation and the complexity of the slip rate function, but also how different arrays can enlighten different aspects of the same rupture process. Using a 1D source allows us to represent the BP image of the rupture as a 2D map where we can easily follow the HF progression in space and time, drawing the attention to the mechanism behind the generation of high-frequency radiation from spatial heterogeneities in the kinematic rupture parameters.

After developing a conceptual understanding of the relation between the BP image and the variability of the parameters controlling the rupture process, we move on to adopting a convolutional neural network (CNN) approach to look for the statistical link between the BP images and the rupture kinematic parameters, exploring the role of input and target parameters on the accuracy of the CNN predictions. In particular, we aim to assess which kinematic characteristics of the rupture process, as well as the location and the extent of a spatial heterogeneity —when present— can be reliably determined from the BP image of the seismic event.

2. Methodology

2.1 *The line source model*

The line source is an intermediate approach between the point source and the extended source model (Lancieri and Zollo 2009). Its advantage lies in the ability to reproduce the typical 2D-source directivity effects on the signal while requiring a lower computational effort. Use of this model is most appropriate for earthquakes with aspect ratios (fault length divided by width) well in excess of one, such as for large strike slip earthquakes and great subduction zone earthquakes. Our source model is built by placing a series of equally spaced point sources along a line (with total length equal to the fault length). These points are set at the hypocentral depth of the event and are distributed along the strike direction of the fault. The point sources begin to slip at different subsequent activation times, related to the rupture propagation velocity along the line. Once crossed by the rupture front, each point source slips following a ramp function whose duration is the rise time. We describe the line source model with the following parameters:

- the hypocentral coordinates of the seismic event;
- the strike direction of the fault;
- the rupture length L;
- the rupture velocity Vr along the line;
- the discretization along the line ΔL;
- the rise time t_r, or the duration of the dislocation, for each point source;
- the final slip value s_f, reached by each point source at the end of the dislocation.

Under the line source approximation, each point has the same focal mechanism (slip vector and fault orientation) and the total seismic moment of the event is given by the sum of the seismic moments of each point source. An estimation of the fault length (L) and width (W) is derived from the event magnitude using, e.g., the Wells and Coppersmith (1994) empirical relationships. To avoid space-time aliasing, the contributions emitted by each elementary source must overlap in time; i.e., the duration of each elementary source (the rise time) must be greater than the time the rupture takes to propagate to the next source (here called τ), as discussed in Lancieri and Zollo (2009). To properly set the point source spacing along the line, different simulations were performed, leading to the optimal sampling assigned in **table 1**.

Table 1: *Hypocentral coordinates and focal mechanism of the Mw = 7.8, 2001 Kunlun earthquake, used as a frame for our synthetic study. Rupture length L and width W derived from Wells and Coppersmith empirical relations. Space ΔL and time Δt sampling chosen in order to avoid space-time aliasing, as discussed by Lancieri and Zollo (2009). P- and S- wave velocities and quality factor used for the Green's fuctions.*

Hypocentral Coordinates (°)	**Focal Mechanism (°)**
Lon = 90.59, Lat = 35.93	Strike = 78, Dip = 61, Rake = -12
Hypocentral depth (km)	**Rupture Geometry (km)**
Z = 13	L = 100, W = 15
P-wave velocity (km/s)	**Space sampling (km)**
$\alpha = 5.8$	$\Delta L = 0.4$ km
S-wave velocity (km/s)	**Time sampling (s)**
$\beta = 3.46$	$\Delta t = 0.02$ s
Attenuation	
Q = 730	

In the present study, we locate the earthquake in Northwestern China, and we use the geometry of the Mw = 7.5, 2001 Kunlun earthquake (Klinger et al. 2005, Vallée et al. 2008). The generated source models do not aim at reproducing the exact rupture process of the Kunlun event, but they rather explore different rupture scenarios. However, our synthetic model does share the same hypocentral coordinates, seismic moment, focal mechanism and rupture propagation direction of the Mw 7.5, Kunlun earthquake, as summarized in **table 1**. Hypocentral coordinates and focal mechanism are obtained from the Global CMT Moment Tensor Solution (Dziewonski et al, 1981). We simulate 40,000 rupture scenarios of the Mw 7.5 strike-slip event adopting the 1D line source model with large range of complexity. To capture a range of different scenarios, we vary the kinematic parameters (rise time, final slip and rupture velocity) for each simulation. Each kinematic parameter is randomly selected within a range of values shown in **table 2** according to the empirical relationships proposed by Wells and Coppersmith (1994) and Geller (1976). In addition, we introduce a heterogeneous segment whose length L_H ranges from one space sample, that is 400 m, to 40 km. Within the heterogeneous segment, the rise time, the final slip and the rupture velocity assume a different value from the surrounding length.

Table 2: *Ranges of kinematic parameters for rupture process simulation. We call t_r the rise time, s_f the final slip, Vr the rupture velocity, L_H the length of the heterogeneous segment and x_c its central position. Kinematic parameters are uniformly distributed within the range listed below.*

tr (s)	Sf (m)	V_r(m/s)	L_H (km)	X_c (km)
1-8	1-10	2500-3460	0.4-40	20-80

2.2 Modeling body waves at teleseismic distance

For each rupture scenario generated in the previous section, we compute synthetic seismograms at three arrays of seismic stations at teleseismic distances (between 50 and 90 degrees): Alaska (AK), Europe (EU), and Australia (AU). Each array is comparable to an antenna that tracks in space and time the strongest coherent sources of HF seismic energy. The arrays are located at three complementary locations with respect to the epicenter of the event, allowing us to obtain three different viewpoints of the same rupture process. Each array is composed of 55 stations (black triangles in **Fig.1**). The interest of working at teleseismic distances lies in the possibility of investigating high-frequency emissions using only the far-field term of the Green's function in the representation theorem (Aki and Richards, 1980). This approximation leads to many simplifications of the calculations and simple physical models of the generation of high-frequency waves. In the current study, the Green's functions are calculated in a spherically averaged Earth's structure AK135 (Kennett et al., 1995). The ground motion associated with the displacement on the fault plane is computed by considering the representation integral in the frequency domain. Here, in particular, teleseismic body waves are computed by taking into account only the direct P arrival and associated depth phases, pP and sP. We compute the displacement associated with a teleseismic P-wave in a geometrical ray solution following the formula of Okal (1992). However, in our study, we neglect the geometrical spreading and the response of both the receiving site and the recording instrument by normalizing the individual traces. To compute the reflection coefficients for pP and sP phases into the synthetic seismograms, we use the calculations made by Aki and Richards (1980). Values for P- and S- wave velocity are shown in **table 1**.

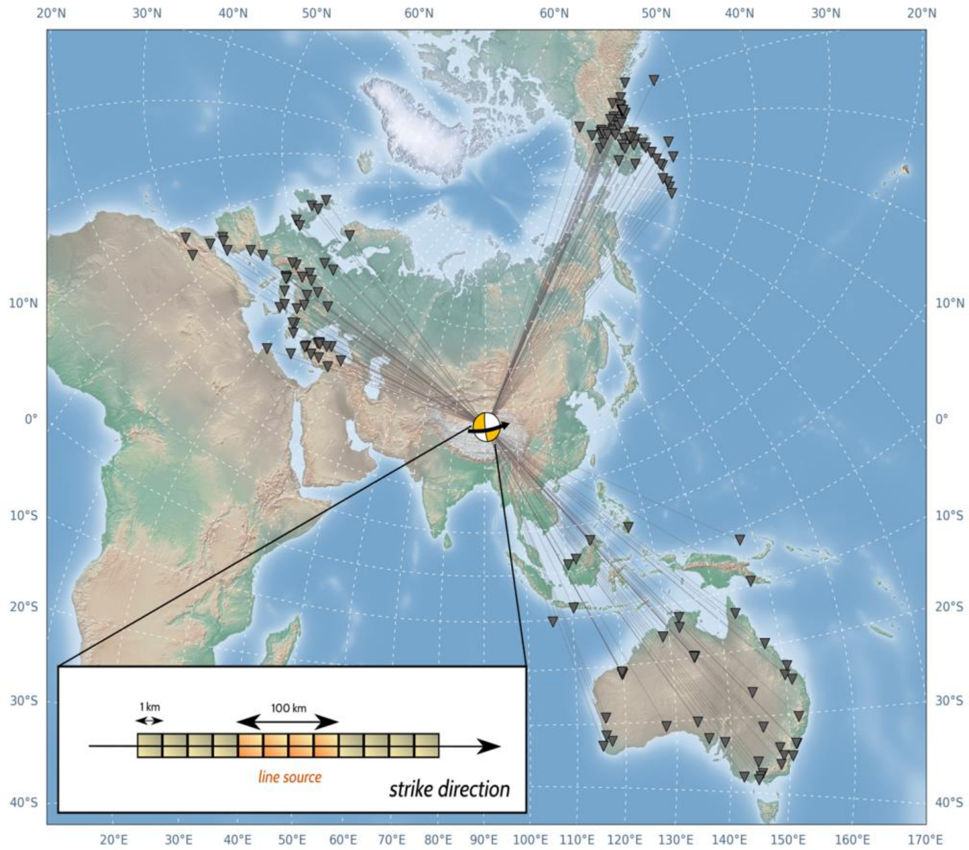

Figure 1: *Geographical setting of the present study. Focal mechanism and epicentral location of the synthetic test are placed in Northwestern China. Alaskan (AK), Australian (AU) and European (EU) arrays are composed each of 55 seismic stations (black triangles). The bottom window shows a zoom over the 300 km long one-dimensional BP grid that surrounds the line source.*

2.3 Description of the synthetic data-set

Our data-set is composed of 55 Z-component synthetic displacement traces for each array in **Fig.1**. The AK and AU arrays are located almost in the directive position respect to the rupture propagation, whereas the EU array is located almost in the antidirective position. To identify high-frequency pulses, the synthetic displacement traces are then differentiated in time and band-pass filtered between 0.5 and 4 Hz. The filter is a zero-phase 4-pole Butterworth, to obtain an acausal filtered signal where the arrival time of the signal's peak is respected.

2.4 Back Projection imaging

We follow the conventional back projection (BP) method for source imaging first proposed by Ishii et al. (2005), where the body waves arriving at an array of recording stations are projected back to a (generally 2D) source grid under the ray-theory asymptotic approximation. To apply the back-projection method, we define the coordinates of the source grid points and assume a velocity model to calculate theoretical travel times. We use a 1D grid of potential source locations placed over the line source. In particular, the grid is 300 km long with a grid-step of 1 km (**Fig.1**) and all grid points are placed at the hypocentral depth. This is a simplification of the standard approach in BP analysis where a two-dimensional grid is used. The BP image is then constructed through the following steps:

1. For each grid-point, theoretical P-wave travel times are calculated at each station of the array in the AK135 velocity model (Kennett 2005);
2. Filtered seismograms are reverse time shifted according to the values of travel times;
3. Shifted traces are stacked, returning a signal related to the grid point. If the shifted traces sum constructively, the stack is high, meaning that the grid point is a plausible source of coherent HF radiation (from the array point of view). If the stack is low, in contrast, the grid point likely did not contribute coherent HF energy during the rupture process.

Several methods exist for aligning and stacking seismic traces, for instance, the Nth root stacking (Muirhead 1968) and the F-ratio (Melton and Bailey 1957). In our study, traces are combined via the shift-and-sum approach, because this linear approach is the simplest technique for combining the station traces, it requires the least a priori assumptions and it does not deform the amplitude of the signals and. Mathematically, the linear stack $\boldsymbol{s_i}$(t) at the i-th potential grid point can be expressed as follows:

$$\boldsymbol{s_i(t) = \sum_j \dot{u}_j \left(t - t_{ij}^P\right)}. \qquad (1)$$

Where $\boldsymbol{\dot{u}_j}$ is the velocity trace at the j-th station and $\boldsymbol{t_{ij}^P}$ is the theoretical P-wave travel time from the i-th source to the j-th station. In the calculation of the BP image, we replaced the stacked signal by its squared value, the beam power. The beam can be highly noisy especially for HF filtered signals, where further peaks appear because of the filter. To further reduce the noise, the beam is smoothed using a zero-phase Gaussian filter, parametrized by its standard deviation σ. We tested different values of Gassuain smoothing windows (σ), and chose the value of σ = 0.4 s, which allows us to only focus on the main energy bursts neglecting the smaller peaks coming from the filtering and stacking procedures.

The resolution of BP images mostly depends on two factors: the frequency content of the data and the geometry of the array. In general, the higher the frequency we are looking at, the more detailed the BP image will be (Schweitzer et al. 2011). Likewise, both the aperture and the position of the array with respect to the rupture direction control the resolution of the BP image. Specifically, good resolution in BP images is achieved when using large-aperture arrays (Xu et al. 2009). Low-frequency ($f < 1$ Hz) P-waves are less affected by scattering and smaller-scale heterogeneity, thus their stack generally returns a high coherency. However, they do not provide a good degree of detail on BP images. On the contrary, HF ($f > 1$ Hz) P-waves provide a high resolution on BP images, but at the same time their waveforms are more easily distorted by small-scale heterogeneity and scattering (e.g., Frankel et al, 1986, Takemura et al., 2013), often leading to a less coherent stack. In addition, similarity among traces breaks down as interstation distance increases (Xu et al. 2009). The frequency range 0.5-4 Hz is indeed typical in BP analysis at teleseismic distance, because it is a good balance between the resolution of the BP image and the waveform coherence (Xu et al. 2009).

2.5 Reducing artifacts in the BP image

In BP analysis there are several potential artifacts that one needs to be aware of. These include “smearing” and the “walking” effects (e.g., Meng et al, 2012, Xu et al. 2009, Walker and Shearer 2009), and the presence of HF emissions carried out by later arrivals, namely the depth phases (Yagi et al, 2012). The smearing effect makes the beam power signal of the true HF emission source to be blurred in space, whereas the walking effect leads to having a false energy radiation appearing before and after the true emission time. In addition, the presence of HF emissions carried out by depth phases can obscure some of the first-order features of the rupture process. Okuwaki et al. (2018) show that BP has a depth-dependent bias proportional to the amplitude of the Green’s function. At shallow depths (e.g., focal depths less than 10 km) these artifacts are caused by non-physical interactions of the back-projected P wave and depth phases. For deep earthquakes, on the contrary, depth phases are separated enough from the direct P-wave and they can be used to constrain depth (Kiser et al, 2011). However, in this case they might still complicate the interpretation of the BP image, as further HF peaks appear in the image, but they are not generated by the complexities of the source.

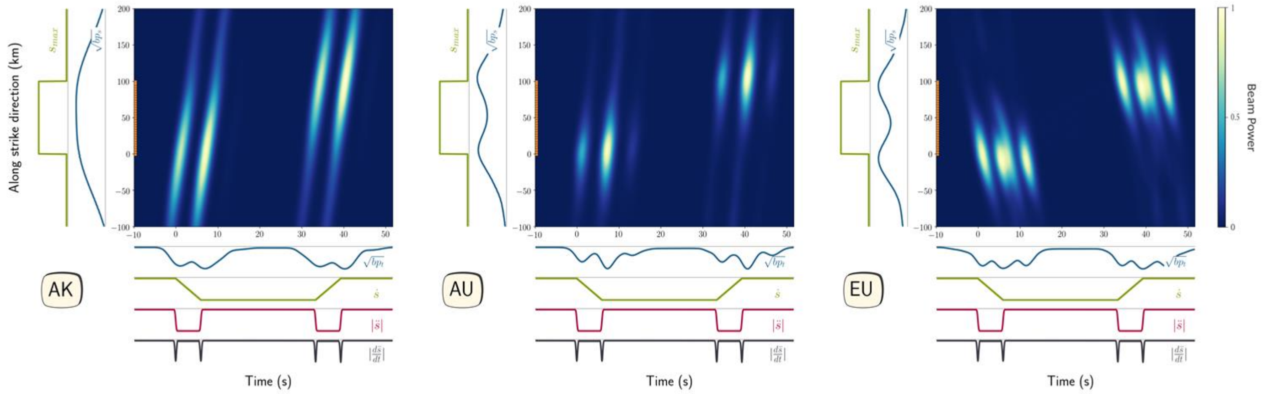

Figure 2: *BP images of a homogeneous rupture process calculated at the three arrays. Time is plotted along the x-axis and the along strike direction is plotted along the y-axis. In the left subplots we show the squared root of the beam power integrated in time (in blue) and the maximum value of the slip-rate function (in green). In the bottom subplots we show the squared root of the beam power integrated in space (in blue), the slip-rate function (in green) and the absolute values of the slip-acceleration function (in red) and its time derivative (in black). The blurred and tilted patches correspond to the BP reconstruction of the HF emissions related to the source complexity and the contamination of the depth phases.*

A current issue in BP analysis is therefore how one can remove the smearing effect and the nonphysical contribution of the depth phases that are incorrectly back-projected by the direct P wave travel times to obtain only the true location of the HF radiation in space and time. In **Fig.2** we show by way of example the BP images of a homogeneous rupture process calculated at the AK, AU and EU arrays using the conventional approach described in Ishii et al. (2005). The figure shows that a few pulses of HF emission retrieved by the BP analysis are found in correspondence with the nucleation and the stopping phases of the rupture. This happens because in a homogeneous rupture process all kinematic parameters are constant along the line fault, and only the nucleation and the stopping phases of the rupture generate abrupt changes in the slip-rate function (see the slip-rate function in the bottom subplot), that in turn produce seismic waves. Hence, the two bursts of HF radiation at the nucleation and at the end of the simulation are an effect of the finite duration of the rise-time. The presence of several pulses of HF emissions both at the nucleation and at the stopping of the rupture is due to the contamination of depth-phases (see in particular the BP image obtained at the EU array). In addition, the HF emissions are also tilted in time depending on the relative position between the array and the rupture direction. Several approaches have been proposed in the attempt to improve resolution and reduce the artifacts in BP images (e.g., Lay et al. 2010, Wang et al. 2012, Haney 2014, He et al. 2015, Nakahara and Haney 2015, Wang and Mori 2016). In the first part of our study, we use the method described in Wang et al. (2016), hereinafter W2016. In their study, the authors propose a two-step procedure, first to correct the time tilt of HF emission patches and second to reduce the smear around the true HF energy peaks. The first step of the approach proposed by W2016 is performed by selecting a reference station lying in a central position within the array. In the conventional BP technique, the signal is shifted by the theoretical travel time t^P_{ij} between the grid point i and the station j. In the approach suggested by W2016, the signal recorded at a station j is shifted by the difference between the travel time at the station j and the travel time at the reference station:

$$\boldsymbol{s_i(t) = \sum_j \dot{u}_j \left(t - \tau^P_{ij}\right)}. \qquad (2)$$

$$\text{and } \boldsymbol{\tau^P_{ij} = t^P_{ij} - t^P_{iJ}}. \qquad (3)$$

where $\boldsymbol{\dot{u}_j}$ is the velocity trace at the j-th station, $\boldsymbol{\tau^P_{ij}}$ is the i-th source travel-time difference between the j-th station and the reference station J. This procedure returns a BP image of the rupture as if it were seen by the reference station, where the HF emissions are no longer tilted in time. However, by following the ‘time correction’ of the approach proposed by W2016, we obtain a BP image where the time axis is no longer the absolute time at the source, but it rather corresponds to the apparent time at the reference station. It is instructive to notice that, in this new reference system, the directivity effect of the source appears in the BP images in terms of time stretching or compression of the HF emissions (see **Supplementary Material**).

Several authors have interpreted the smear around the true HF peaks on BP images as an artifact created by the array, referred to as array response (Xu et al. 2009, Meng et al. 2012, W2016). In particular, in their second step of the approach, W2016 suggest looking at the BP image of an earthquake as a convolution between the BP image of the true HF peaks and the BP image of the array response. The array response can be evaluated in different ways: theoretically, with synthetic Green’s functions (e.g., Rost and Thomas, 2002), or with empirical Green’s functions. The latter is usually performed by applying the BP analysis to a smaller earthquake that can be assumed to be a point source. The procedure proposed by W2016 can also help remove the contamination of depth phases into the BP images. In their study, W2016 use an aftershock as an effective point source and a non-negative least squares (NNLS) algorithm to perform the deconvolution. In our study we use a synthetic point source activating at the hypocenter as array response and perform the deconvolution using the Richardson and Lucy restoration algorithm (Richardson 1972, Lucy 1974), hereinafter R&L. In **Fig.3** we show an example of the R&L restoration algorithm applied to the BP image of a homogeneous rupture process calculated at the EU array. Once the HF peaks have been extracted via the R&L algorithm (**Fig.3c**), we restore the time axis in the BP images from the apparent time of the reference station to the absolute time at the source by inversion of the W2016 time correction equation.

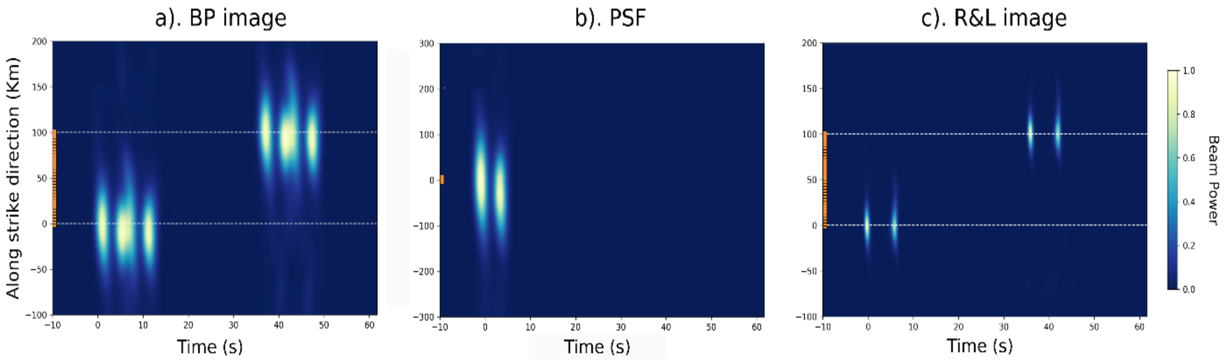

Figure 3: *example of the Richardson and Lucy restoration algorithm applied to the BP image of a homogeneous rupture process calculated at the EU array. (a) Original BP image; (b) PSF obtained as the BP image of a point source activating at the hypocenter; (c) Restoration result after the R&L algorithm.*

3. Relation between BP and fault slip

To better understand the relation between the BP image and the fault slip, we select two representative cases among the 40,000 rupture scenarios:

1) a homogeneous rupture model, where the kinematic parameters are constant along the line;

2) a heterogeneous rupture model, where a segment of 30 km length is introduced in the middle of the fault; within this segment, the rise-time value assumes a different value respect to the surrounding rupture.

3.1 Homogeneous rupture model

In a homogeneous rupture model, the kinematic parameters are constant along the line: the rupture propagates along the line fault with constant velocity and the source points have the same value of rise time and final slip. Specifically, the case we selected presents the following values: rupture velocity V_r = 3 km/s; rise time t_r = 6 s; final slip s_f = 8 m.

In a homogeneous rupture process, the shape of the slip-rate function is extremely simple, and the unique abrupt changes are the slopes associated with the nucleation and stopping of the rupture. An example of teleseismic synthetic traces generated at the three arrays is shown in **Fig.4a**, where the signal is characterized by two abrupt changes, corresponding to the initiation and the stopping of the rupture, whereas the remaining portion of the signal is flat, indicating a constant rupture process. In **Fig.4a** we notice that the HF band-pass filter behaves like a time-derivative on the velocity trace as, more specifically, the pulses on the HF-filtered signal highlight the discontinuities of the velocity trace. In particular, the effect of the finite duration of the rise-time determines a two-pulse HF radiation both for the nucleation and the stopping of the signal. The effect of the depth phases is almost imperceptible on the AK array, because of the radiation pattern. Here, four HF pulses are visible in association with the discontinuities in the slip-rate function due to the nucleation and the stopping phases of the rupture. In contrast, the waveforms at the AU and EU arrays are measurably perturbed by the depth phases. Here, synthetics show at least three pulses for the AU array and four pulses for the EU array.

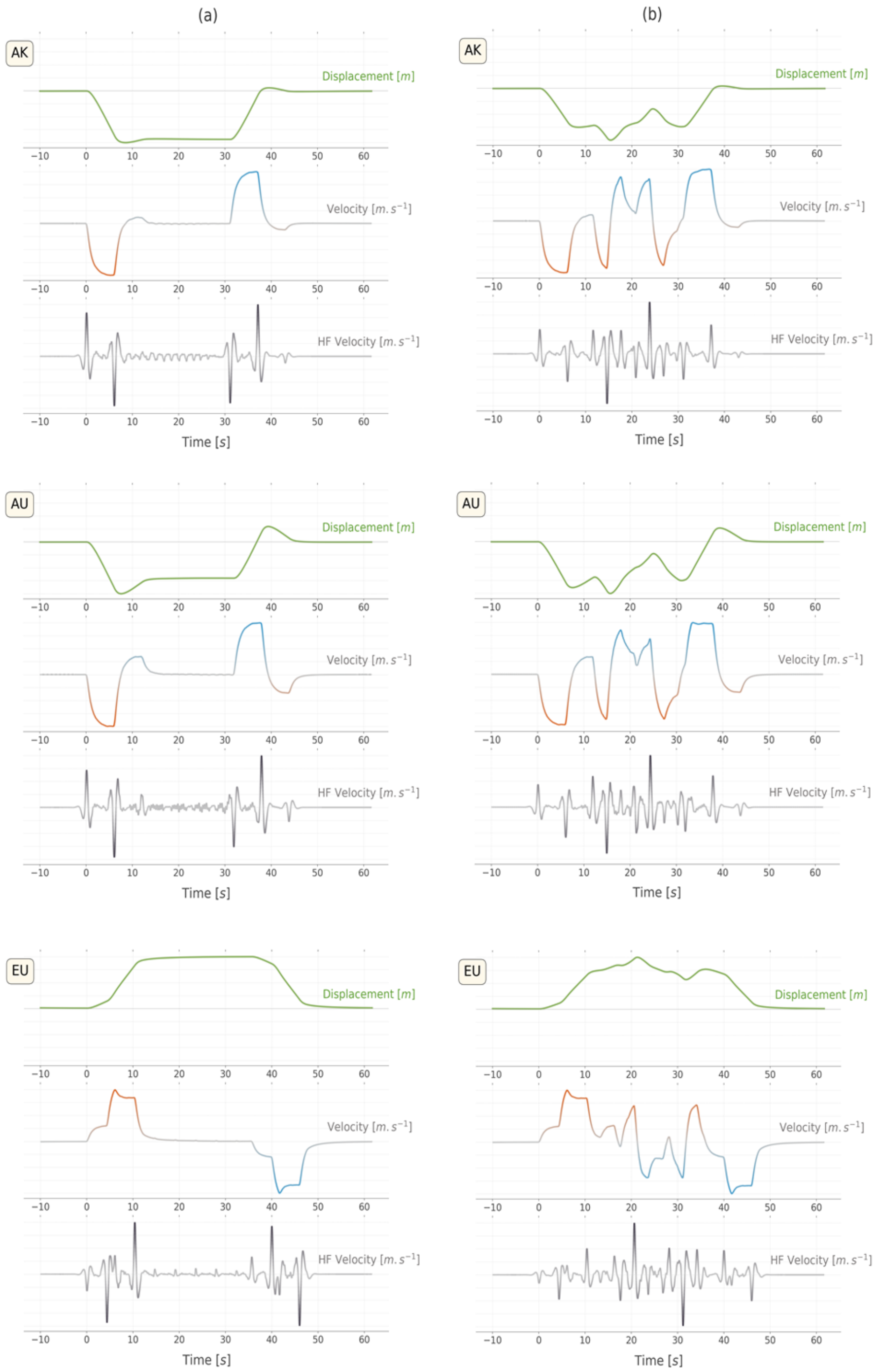

Figure 4: *Example of a teleseismic synthetic trace generated at AU, AK, and EU array for a homogeneous (a) and a heterogeneous (b) rupture process. In each plot, we show the displacement trace on the top, the velocity trace in the middle, and the velocity trace band-pass filtered between 0.5-4 Hz at the bottom.*

In **Fig.5a** we show the location in space and time of the HF peaks obtained via the R&L restoration algorithm to eliminate the contamination of depth phases in the BP images. The three arrays are in agreement in terms of the location of the peaks in space and time and their intensity. Four HF peaks are observed: the first two, generated at the hypocenter, corresponding to the rupture nucleation; the other two, generated at the end of the ruptured segment, corresponding to the rupture stopping. In particular, if we compare the HF peaks with the subplots in time axis, we notice that the HF peaks appear at the discontinuities of the slip acceleration function and are therefore better associated with the absolute value of the time derivative of the slip-acceleration function.

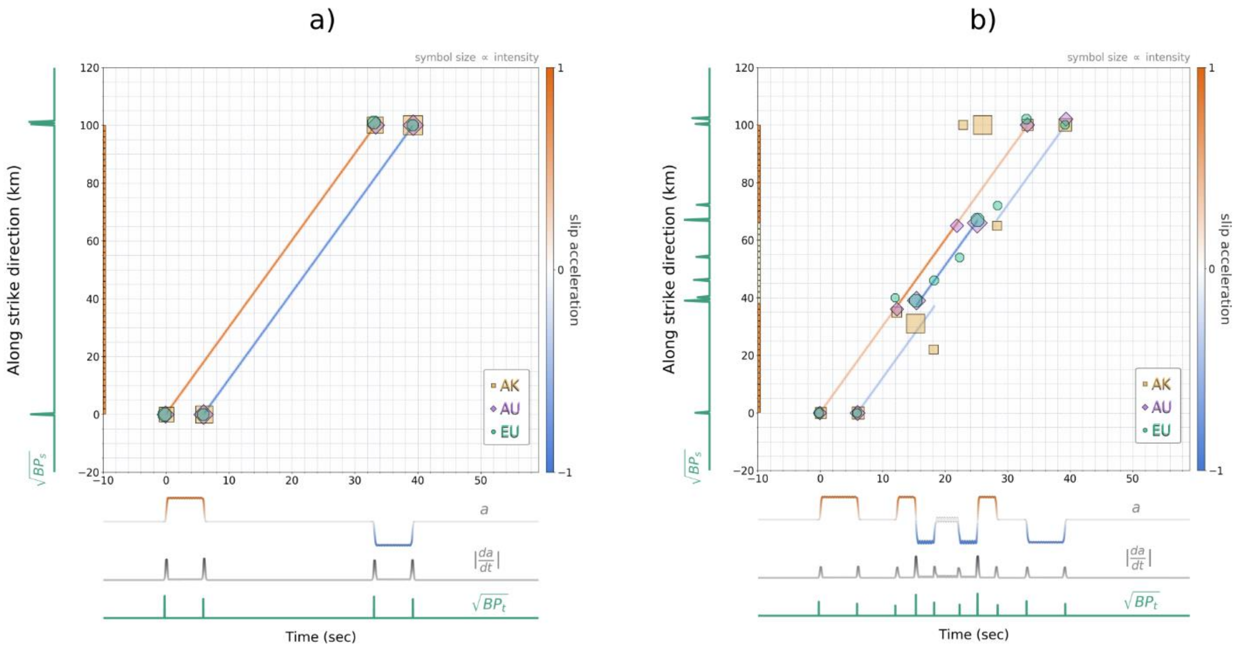

Figure 5: *HF peaks for a homogeneous (a) and a heterogeneous (b) rupture process retrieved at AK, AU and EU array. HF peaks size is proportional to the intensity of the beam power. In the main plot we show the normalized slip-acceleration function. The along strike direction is on the y-axis (in orange we plot the line source) and the time is on the x-axis. The marginal on the left is the squared root of the beam power signal for the EU array. The marginal on the bottom are: the total slip-acceleration function a; its time derivative in absolute value; the squared root of the beam power signal for the EU array.*

3.2 Heterogeneous rupture model

In this heterogeneous case, a 30 km long segment is placed in the middle of the line fault and we change the rise time value for the source points within it. The rupture propagates with constant rupture velocity (Vr = 3 km/s) and the source points reach the same final slip value (s_f = 8 m). The rise time, on the contrary, has an abrupt change from 6 s to 3 s, determining a faster activation of the 'heterogeneous' points. An example of teleseismic synthetic traces for this heterogeneous rupture process generated at the three arrays is shown in **Fig.4b**, where the signals show a higher complexity beyond the nucleation and the stopping of the rupture. In particular, the decrease in the rise time value within the heterogeneous segment produces additional elastic waves, since the slip rate function experiences a transient acceleration when encountering the heterogeneity. Multiple pulses in fact appear on the HF-filtered traces **Fig.4b**: they mark not only the nucleation and the stopping phases, but also the major discontinuities in the slip-rate function due to the location of the heterogeneity.

In figure **Fig.5b**, the three arrays are not always in agreement in terms of the location of the peaks in space and time, neither do they retrieve the same number of peaks. As previously seen in the homogeneous rupture process, HF peaks are again observed at the hypocenter, corresponding to the rupture nucleation, and at the end of the ruptured segment, corresponding to the rupture stopping. Additional HF peaks appear at the edges of the heterogeneous segment in space, and they match the discontinuities of the slip acceleration function in time. The result of the peak extraction following the R&L restoration algorithm is not optimal for the AK array, whereas it works better for the AU and EU arrays. For the EU array in particular, the beam power closely matches the absolute value of the time derivative of the slip-acceleration function. Along the strike direction, the localization of the peaks is good for the hypocenter and the end of the ruptured segment, whereas the localization of the peaks generated by the presence of the heterogeneous segment is not always clear. The rise time, on the contrary, has an abrupt change from 6 s to 3 s, determining a faster activation of the 'heterogeneous' points.

4. A Convolutional Neural Network approach

The second step of this work is to understand the statistical link between the BP image of an earthquake and the kinematic parameters controlling the rupture process. Here we apply a CNN approach to the 40,000 BP images of the rupture scenarios previously generated. To take full advantage of the features contained in the BP image, whether they be artifacts or true source emissions, for each rupture process we calculate the BP image using the conventional approach by Ishii et al. (2005). In the calculation of the BP image, we replace the stacked signal by its squared value, the beam power. However, in this second part of our study, we want to apply a minimal pre-processing and allow the CNN to find the best link between the BP image and the kinematic parameters. Hence, hereafter the beam is not smoothed with a Gaussian filter and, most importantly, no peak extraction or other manipulation is made on the BP images. Finally, we apply a CNN approach to exploit the information carried by the HF radiation in the BP images and to understand the relation between the features and the kinematic parameters.

4.2 CNN architecture

The CNN is a regression model that is trained in a supervised way and therefore needs an input and a target. In our study, the input is a 2D matrix containing the pixels of the BP images of the simulated rupture processes, and the target is a 1D vector containing the kinematic parameters corresponding to those simulations. Specifically, the target vector d is defined as:

$$\boldsymbol{d = [t_r, s_f, V_r, H_{tr}, H_{sf}, H_{Vr}, x_c, L_H].} \qquad (4)$$

where t_r is the rise time, s_f is the final slip, V_r is the rupture velocity; H_{tr} , H_{sf} and H_{Vr} are the heterogeneities respectively in the rise time, in the final slip and in the rupture velocity; x_c and L_H are the central position and the length of the heterogeneous segment. The objective of the CNN algorithm is to learn from data a functional mapping between the input matrix and target vector (LeCun et al., 1998, Goodfellow et al. 2016).

We tested various network architectures in our study. Our preferred one has the structure sketched in **Fig.6**, because it required a smaller number of learnable parameters (improving its generalization performance) and was computationally efficient in training. In this architecture, the BP image is first downsampled with a max-pooling operation, with equal pooling lengths of [3] w × [3] h along the image dimensions. Once downsampled, the BP image is passed through two convolutional layers, each with a convolution, a max-pooling, and an activation function. The convolution is performed with 5 and 10 filters, in the first and second layers, respectively. The kernel size for both layers is [5] w × [5] h. The max-pooling operation is performed with pooling lengths of [4] w × [4] h in the first layer and of [3] w × [3] h in the second layer of the loop. A rectified linear unit (ReLu) (Ramachandran et al. 2017) is used as an activation function. Two fully-connected layers link these convolutional layers with the output target (**Fig.6**). We refrain from using a large number of convolution and pooling layers, as is common in CNN applications, because we want to preserve a substantial portion of the space-time axes of the image, since we infer that space-time resolution is important in back-projection analysis to back-out the relevant kinematic parameters. Network weights are updated during the learning to minimize the loss function, in our case, we use the mean squared error (MSE):

$$MSE = \frac{1}{M}\sum_{n=1}^{M}(d_n - y_n)^2. \tag{5}$$

where M is the number of samples in the dataset, d_n is the normalized target vector containing the true kinematic parameters for the sample n, y_n is the normalized output vector containing the prediction of the kinematic parameters for the sample n. The kinematic parameters used in the simulations are uniformly distributed, hence we adopt a min-max normalization on target data to map them to the range 0 to 1:

$$\tilde{d}_n = \frac{d_n - \min(d)}{max(x) - min(x)}. \tag{6}$$

where $\tilde{\boldsymbol{d}}_{\boldsymbol{n}}$ is the normalized target. During the training, the updates to the model weights are controlled by the learning rate, which quantifies how fast the model adapts to the problem. In our study, we initialize the weights using the Glorot initialization scheme and set the learning rate equal to 7.5×10^{-5}. The Adam algorithm (Kingma and Ba 2014), applied in the PyTorch framework (Paszke et al., 2017), is used to train the networks. The original dataset composed of 40,000 simulations of rupture processes is divided into three subsets: training (70%), validation (20%) and testing (10%). The network is trained for up to 500 iterations over the training dataset. The model's parameters for which the MSE reaches its minimum during the validation step are then selected as the best model's parameters which will be used for the testing.

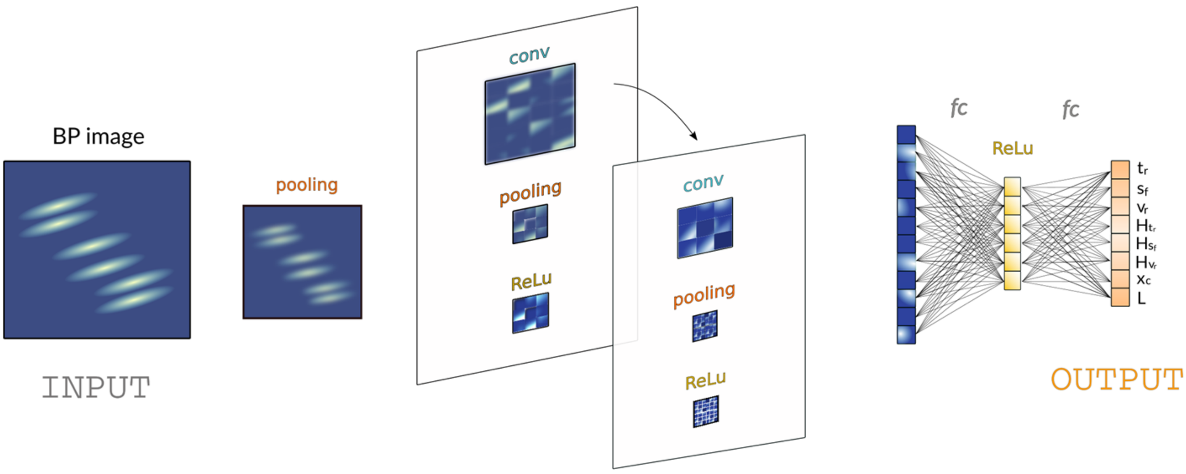

Figure 6: *Sketch illustrating the design of the CNN used in the present study. The input is the BP image which undergoes a max pooling operation first. Then, once downsampled, the BP image is passed through two convolutional layers, each composed of a convolution (conv), pooling and activation (ReLu) operation. The network ends with a two fully-connected layers (fc). The output of the network is the vector containing the kinematic parameters of the rupture process.*

5. Statistical link between the BP image and the target parameters

5.1 Effect of target on CNN predictions

In **Fig.7** we present the results obtained with the design of the CNN sketched in **Fig.6** and the target vector defined in (4). We include outputs of both the stacked version of the method (sum of the BP images obtained from the three arrays), and the predictions for using each array separately. The plots show the output of the CNN versus the target values, which are the predictions of the CNN versus the true values of kinematic parameters, for the testing dataset. To summarize the prediction accuracies, we calculate the regression score function, R^2, for each of the different components of the target vector. This score is defined as:

$$\boldsymbol{R^2 = 1 - \frac{\sum_{i=1}^{n}(d_i - y_i)^2}{\sum_{i=1}^{n}(d_i - \hat{d})^2}}. \qquad (7)$$

where d is the target vector, y is the CNN prediction and $\boldsymbol{\hat{d}}$ is the mean value of the target. This score captures how well the model is able to return a prediction close to the target parameter in a linear regression setting. Its range of possible values is (-1, 1], where the best possible score is 1.0 and a score of 0.0 implies the model predictions are no better than a simple guess based on the average value. A negative value for R^2 implies the model predicts worse than the simple guess. The highest values of R^2 are found for the predictions of the rise time t_r ($R^2 = 0.912$) the rupture velocity V_r ($R^2 = 0.914$) and the central position of the heterogeneous segment x_c ($R^2 = 0.885$). Accurate predictions are also obtained for the heterogeneous values in rise time and rupture velocity, H_{tr} ($R^2 = 0.576$) and H_{vr} ($R^2 = 0.499$). However, the length of the heterogeneous segment L_H is not well predicted ($R^2 = 0.355$) and poor predictions are obtained for the final slip s_f ($R^2 = 0.123$) and its heterogeneous values H_{sf} ($R^2 = 0.017$). We attribute this shortcoming to the inherent insensitivity of the BP approach to image the low-frequency aspects of the rupture process.

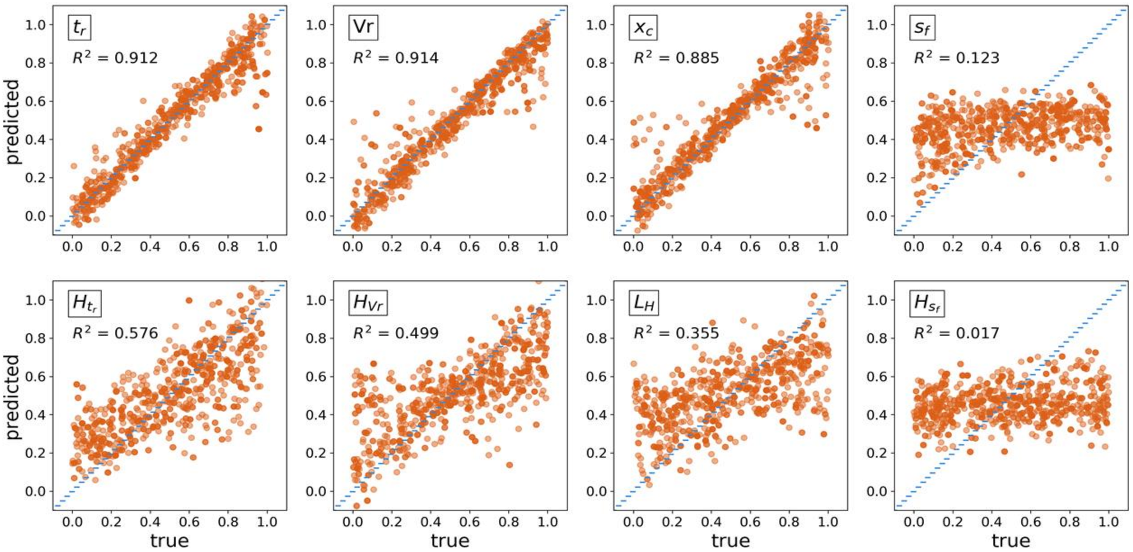

Figure 7: *Predictions of the CNN versus the true values of kinematic parameters, for the testing dataset. The regression score function R 2 is shown in each subplot. The input BP image is obtained as the sum of the BP images calculated at the three arrays AK, AU and EU. We adopt a min-max normalization on target data to map them to the range 0 to 1.*

Difficult-to-predict parameters in the target vector slow down the loss function's convergence towards its minimum. Therefore, we define a different target vector, where we remove the final slip value and its heterogeneity and keep the following kinematic parameters:

$$d = [t_r, V_r, H_{tr}, H_{Vr}, x_c, L_H]. \qquad (8)$$

In **Fig.8** we show the prediction versus the true values of the reduced target vector in (8). The weights for each output channel are independent, therefore the performance on the remaining parameters does not change significantly with a different choice of target vector.

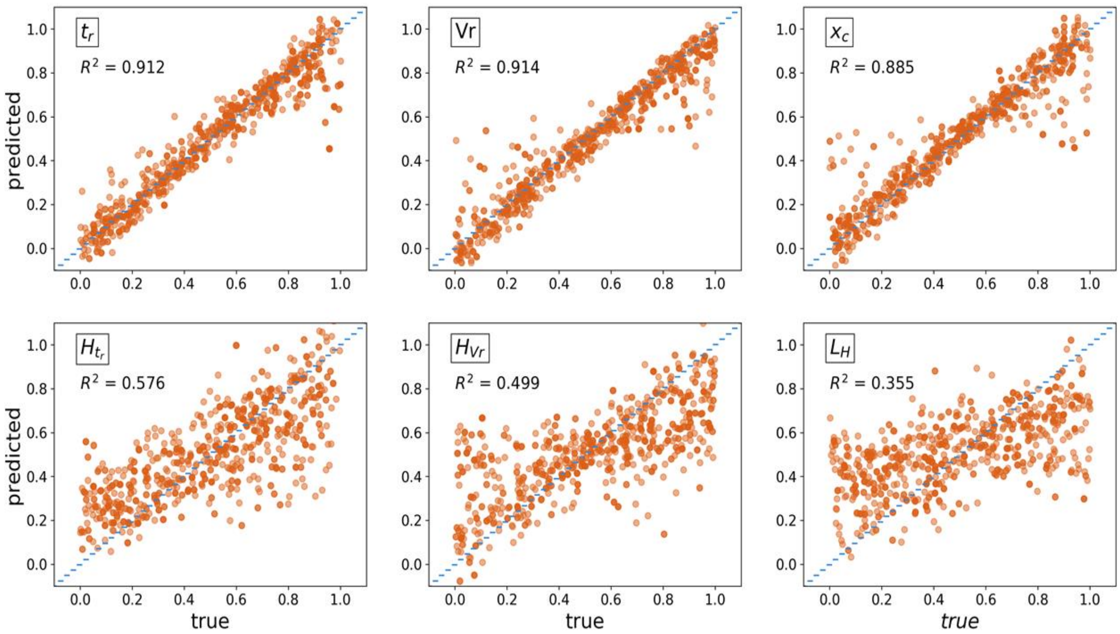

Figure 8: *Predictions of the CNN versus the true values of kinematic parameters of the reduced target vector for the testing dataset. The input BP image is obtained as the sum of the BP images calculated at the three arrays AK, AU and EU. Target data have been scaled to 0-1 via min-max normalization.*

5.2 Effect of input on CNN predictions

As complementary information, we test the effect of the input parameter on the CNN results. In the previous cases, the input of the CNN was a matrix containing the BP images of the simulated rupture processes, obtained as the sum of the BP images calculated at the three arrays AK, AU and EU. Here, we test whether the combination of the three arrays or the employment of only one array at a time in the CNN approach could help us achieve better results.

In **Fig.9** we present the comparison between the results of the CNN approach applied to the sum of the BP images and to the single-array BP image using the reduced target vector. It is instructive to notice that not all arrays perform the same. In particular, slightly better predictions of the rise time and its heterogeneous value can be found when using the BP image of the AK array. The comparison also shows an improvement in the predictions of the length of the heterogeneous segment when we use an input BP image calculated at the EU array. On the contrary, when using the AK or the AU array in isolation, the predictions of the reduced target vector do not improve in comparison to the initial test where the input is the sum of the three BP images. In these cases, the smearing or the walking effect on BP images may hamper the accuracy of the CNN predictions. In our case, the EU and AU array response functions are quite focused along the space direction, whereas the AK array shows higher smearing. The EU array shows the strongest walking effect, because of its large back-azimuth, whereas the HF emissions on AK and AU BP images are not very tilted in time (see as an example the **Fig.2**). However, only the EU array allows the CNN to return the best predictions of the length of the heterogeneous segment, even better than the outputs obtained with the summed BP image. On the contrary, both AK and AU arrays perform worse than the summed BP image for the length of the heterogeneous segment. Even though the smearing effect could encumber the ability of the network to extract information on the BP images, we can't attribute to it the shortcomings of the CNN on AK and AU arrays.

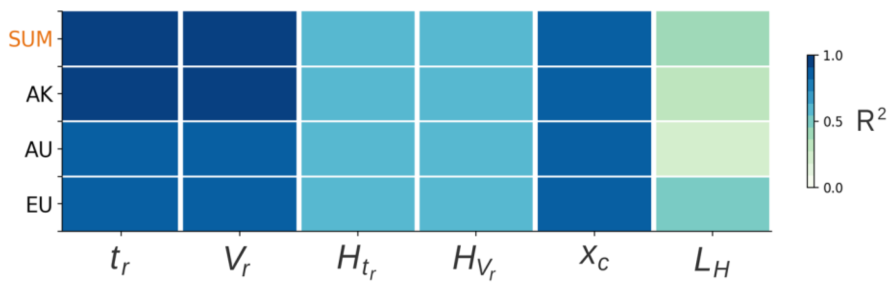

Figure 9: *Regression score function (R2) for the CNN predictions of the kinematic parameters in the reduced target vector when using the sum of the three BP images (on the top) or the single-array BP image as input for the network. The score represents the quality of the model indicating how close the predictions are to the target parameters in a linear regression setting.*

We question, therefore, whether the different performances of the CNN on individual arrays could be attributable to the back-azimuth of the array relative to the rupture. In the conventional BP analysis, the delay-and-sum approach does not carry directivity effects in the duration of the rupture, nor in the time separations between HF pulses in the BP image. Hence, the time axis of the BP image is not affected by the relative position between the rupture direction and the array position. Nevertheless, different tilt angles for the smeared HF radiations are seen in the BP images depending on the back-azimuth. Because of the array configuration and position respect to the rupture direction, coherence among traces can vary from one array to another, determining a different pattern of HF peaks in the BP image among arrays at complementary azimuths [e.g., Xu et al. (2009)]. As a further analysis, we investigate whether the back-azimuth and thus the different HF emission pattern and tilt in the BP image, can favor or restrain the quality of the CNN predictions. We focus the analysis on the EU array because of its strong walking effect. We rotate the previously used line source at nine different azimuths ranging from 0°, being the azimuth of the EU array reference station, to 320°. For each azimuth, we generate 40,000 rupture scenarios and apply the CNN method on them. In **Fig.10** we show the prediction of the CNN for the parameters in (6) and compare the quality of the CNN prediction obtained at nine different azimuths. For each kinematic rupture parameter, we highlight in orange the variability of R^2 as a function of azimuth in the corresponding regression score color-bar. From this analysis, we can notice that the central position of the heterogeneous segment is the best retrieved parameter for all azimuths, whereas the length of the heterogeneous segment shows the widest range of regression scores. But even this range is rather modest [0.35 to 0.50], suggesting that azimuthal changes have a minimal effect on the quality of the CNN predictions.

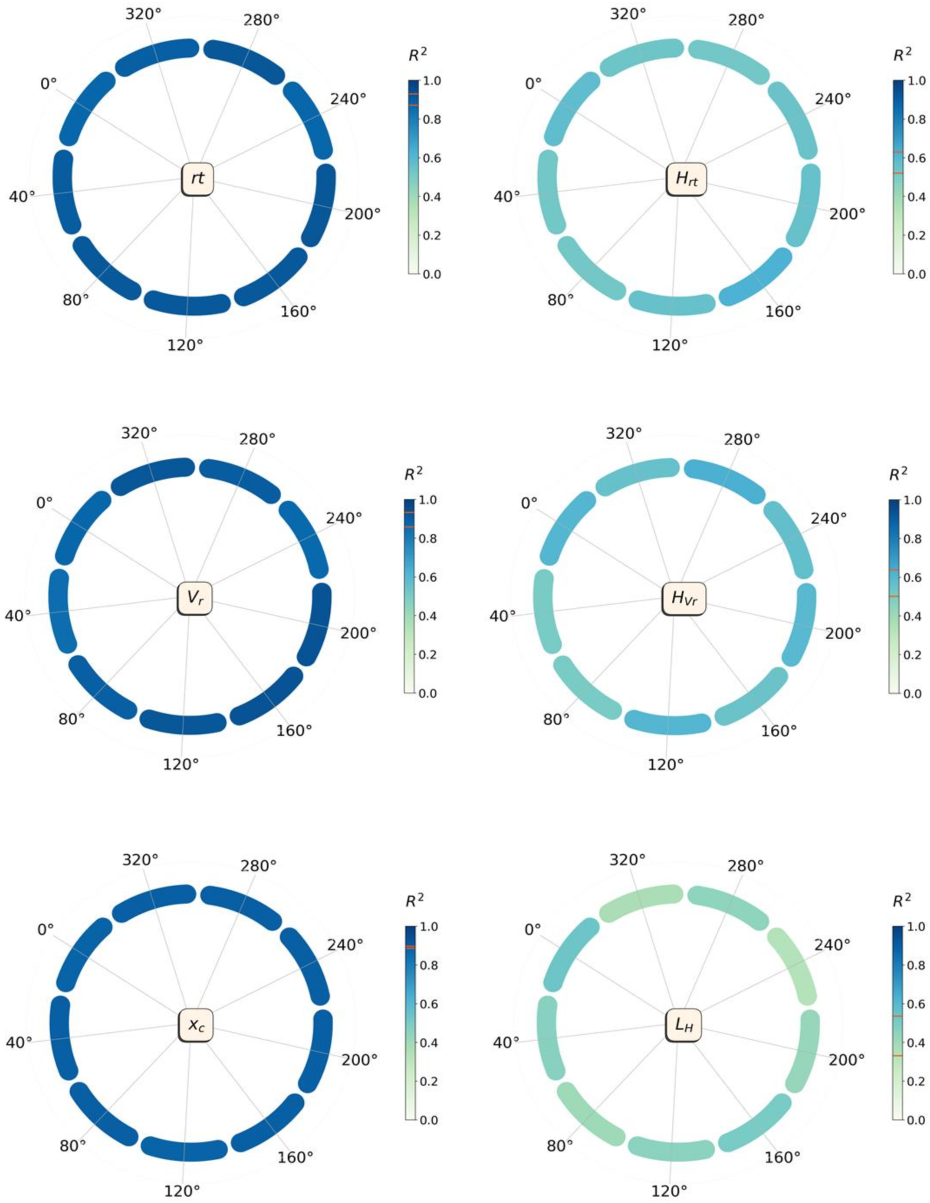

Figure 10: *Azimuthal dependence of CNN predictions for the kinematic parameters in the reduced target vector. The variability of the regression score is represented with an orange interval. For this test the EU array is used and 0° is the back-azimuth of the EU array respect to the line fault strike.*

6. Discussion and Conclusion

The objective of this study was to investigate the link between BP images and the kinematic parameters of the rupture, and, in particular, slip motion on the fault (velocity or acceleration). For this purpose, we studied a large data set of synthetic line rupture processes, characterized by a heterogeneous segment (in terms of final slip, rise time or slip velocity) with variable length and position. Synthetic traces, filtered between 0.5 and 4 Hz, are back projected following the approach of Wang et al. (2016) and the HF peaks are retrieved through deconvolution between the BP image and the array response function (ARF) for the given frequency range. For the particular horizontal line-source configuration chosen here, depth phases strongly contaminate BP images, introducing, for each HF peak, two "ghost" peaks associated with pP and sP phases. Deconvolution with an ARF that includes depth phases restores the original number of peaks with good time accuracy, but sometimes shifts the peaks in space. The role played by depth phases is amplified by the simple horizontal line source geometry chosen here, where all the fault points lay at the same depth. For a more realistic 2D fault, the recording stations will "see" at a given time the energy emitted from different points along a fault isochrone (Bernard and Madariaga, 1984; Spudich and Frazer, 1984) which are generally incoherent and lay at different depths (the isochrone for a line source is a single point). Moreover, the spatial extension of the ARF introduces a further averaging scale which should reduce the coherency of depth phases. The resolution of BP becomes very poor at depth, hence improved BP techniques such as the hybrid BP proposed by Yagi et al. (2012) could be useful in mitigating the effect of depth phases on BP images of 2D synthetic fault models. An important question is whether BP images are associated with slip velocity or acceleration (Fukahata et al., 2014). Here we show that filtering plays an important role, since the 0.5-4 Hz band-pass filter, typically used in BP analyses (Xu et al., 2009) behaves like a time derivative for the seismograms. Comparison between HF peaks extracted from BP images with the slip rate and slip acceleration function, shows that the beam power is more likely to be related to the absolute value of the time derivative of the slip acceleration function, when narrow-band filtering is used. The ability of BP images to retrieve the rupture kinematic parameters was tested using a CNN approach on BP images. CNN are data-driven predictive models, whose performance depends on the definition of input and target parameters. We found that the CNN is able to predict the rise time, the rupture velocity, the heterogeneous values in rise time and rupture velocity, the length and the central position of the heterogeneous segment. However, the CNN fails at predicting the final slip and its heterogeneous value. We attribute this shortcoming to the inherent insensitivity of the BP approach to the low-frequency aspects of the rupture process. We also tested whether the information coming from one single array could be thorough for the network or, on the contrary, if the combination of the information coming from the three arrays could provide us with better predictions. In particular, we tested whether the back-azimuth of the array relative to the rupture could influence the quality of the CNN predictions. Our analysis shows no strong azimuthal dependence in the quality of the CNN predictions depending on the relative position between the source and the array. Thus, from a CNN perspective, stacking multiple arrays may not always provide the best outcome, in contrast to what is more common place in teleseismic BP analysis. It is worth noting that we trained our CNN on a simplistic case of a line source, with the objective to assess the resolving power of BP in a controlled test. Generalization of our CNN approach will require training the CNN on more realistic 2D source models, e.g., using fractal slip distribution (Ruiz et al., 2011), dynamic modeling or real earthquakes.

Even though our study does not fully address the question of the generalizability of the CNN method, it does demonstrate the potential upsides of machine learning approaches in providing reasonably accurate predictions for the other kinematic parameters of the rupture process, which can open a field for its use. Further analysis on the waveform content of synthetic data, as well as a careful analysis on the similarity between the BP images of real data and synthetic data in a fixed frequency band, would enrich our study, potentially making it a suitable approach for real data too, as long as waveforms are carefully pre-processed.

References

Aki, Keiiti, and Paul G. Richards. Quantitative seismology. 2002.

Andrews, D. J. (1981), A stochastic fault model: 2. Time-dependent case, J. Geophys. Res., 86(B11), 10821–10834, doi:10.1029/JB086iB11p10821.

Bernard, P. and Madariaga, R. (1984). High-frequency seismic radiation from a buried circular fault. Geophysical Journal International, 78(1):1–17.

Dziewonski, A. M., T.-A. Chou and J. H. Woodhouse, Determination of earthquake source parameters from waveform data for studies of global and regional seismicity, J. Geophys. Res., 86, 2825-2852, 1981. doi:10.1029/JB086iB04p02825

Frankel, A., and Clayton, R. W. (1986), Finite difference simulations of seismic scattering: Implications for the propagation of short-period seismic waves in the crust and models of crustal heterogeneity, J. Geophys. Res., 91(B6), 6465–6489, doi:10.1029/JB091iB06p06465

Yukitoshi Fukahata, Yuji Yagi, Luis Rivera, Theoretical relationship between back-projection imaging and classical linear inverse solutions, Geophysical Journal International, Volume 196, Issue 1, 1 January 2014, Pages 552–559, https://doi.org/10.1093/gji/ggt392

Goodfellow, Ian, Yoshua Bengio, and Aaron Courville. Deep learning. MIT press, 2016.

Grandin, R., Vallée, M., Satriano, C., Lacassin, R., Klinger, Y., Simoes, M., and Bollinger, L. (2015), Rupture process of the $M_W = 7.9$ 2015 Gorkha earthquake (Nepal): Insights into Himalayan megathrust segmentation, Geophys. Res. Lett., 42, 8373–8382, doi:10.1002/2015GL066044

Haney, Matthew M. "Backprojection of volcanic tremor." Geophysical Research Letters 41.6 (2014): 1923-1928.

He, X., Ni, S., Ye, L., Lay, T., Liu, Q., & Koper, K. D. (2015). Rapid seismological quantification of source parameters of the 25 April 2015 Nepal earthquake. Seismological Research Letters, 86(6), 1568-1577.

Herrero, A., and P. Bernard. "A kinematic self-similar rupture process for earthquakes." Bulletin of the Seismological Society of America 84.4 (1994): 1216-1228.

Ide, Satoshi. "Source process of the 1997 Yamaguchi, Japan, earthquake analyzed in different frequency bands." Geophysical research letters 26.13 (1999): 1973-1976.

Ishii, M., Shearer, P. M., Houston, H., & Vidale, J. E. (2005). Extent, duration and speed of the 2004 Sumatra–Andaman earthquake imaged by the Hi-Net array. Nature, 435(7044), 933-936.

Kennett, B.L.N., Engdahl, E.R. and Buland, R. (1995), Constraints on seismic velocities in the Earth from traveltimes. Geophysical Journal International, 122: 108-124. doi:10.1111/j.1365-246X.1995.tb03540.x

Kingma, D.P., & Ba, J. (2014). Adam: A Method for Stochastic Optimization. CoRR, abs/1412.6980.

Kiser, Eric, and Miaki Ishii. "Back-projection imaging of earthquakes." Annual Review of Earth and Planetary Sciences 45 (2017): 271-299.

Kiser, E., Ishii, M., Langmuir, C. H., Shearer, P. M., and Hirose, H. (2011), Insights into the mechanism of intermediate-depth earthquakes from source properties as imaged by back projection of multiple seismic phases, J. Geophys. Res., 116, B06310, doi:10.1029/2010JB007831.

Klinger, Y., Xu, X., Tapponnier, P., Van der Woerd, J., Lasserre, C., & King, G. (2005). High-resolution satellite imagery mapping of the surface rupture and slip distribution of the M w∼ 7.8, 14 November 2001

Kokoxili earthquake, Kunlun fault, northern Tibet, China. Bulletin of the Seismological Society of America, 95(5), 1970-1987.

Koper, K. D., Hutko, A. R., & Lay, T. (2011). Along-dip variation of teleseismic short-period radiation from the 11 March 2011 Tohoku earthquake (Mw 9.0). Geophysical research letters, 38(21).

Lancieri, M., & Zollo, A. (2009). Simulated shaking maps for the 1980 Irpinia earthquake, Ms 6.9: Insights on the observed damage distribution. Soil Dynamics and Earthquake Engineering, 29(8), 1208-1219.

Lay, T., Ammon, C. J., Kanamori, H., Koper, K. D., Sufri, O., & Hutko, A. R. (2010). Teleseismic inversion for rupture process of the 27 February 2010 Chile (Mw 8.8) earthquake. Geophysical Research Letters, 37(13).

Lay, Thorne, et al. "Depth-varying rupture properties of subduction zone megathrust faults." Journal of Geophysical Research: Solid Earth 117.B4 (2012).

Lucy, L. B. (1974). An iterative technique for the rectification of observed distributions. The astronomical journal, 79, 745.

Madariaga, R. (1977). High-frequency radiation from crack (stress drop) models of earthquake faulting. Geophysical Journal International, 51(3), 625-651.

Mai, P. Martin, et al. The earthquake-source inversion validation (SIV) project. Seismological Research Letters, 2016, 87.3: 690-708.

Melton, B. S. and Bailey, L. F. (1957). Multiple signal correlators. Geophysics, 22(3):565–588.

Mendoza, C., & Hartzell, S. H. (1988). Aftershock patterns and main shock faulting. Bulletin of the Seismological Society of America, 78(4), 1438-1449.

Meng, L., Ampuero, J.-P., Luo, Y., Wu, W., and Ni, S. (2012). Mitigating artifacts in back-projection source imaging with implications for frequency-dependent properties of the tohoku-oki earthquake. Earth, planets and space, 64(12):5

Meng, L., Inbal, A., & Ampuero, J. P. (2011). A window into the complexity of the dynamic rupture of the 2011 Mw 9 Tohoku-Oki earthquake. Geophysical Research Letters, 38(7).

Muirhead, K. (1968). Eliminating false alarms when detecting seismic events automatically. Nature, 217(5128):533

Nakahara, Hisashi, and Matthew M. Haney. "Point spread functions for earthquake source imaging: an interpretation based on seismic interferometry." Geophysical Journal International 202.1 (2015): 54-61.

Okal, E. A. (1992). A student’s guide to teleseismic body wave amplitudes. Seismological Research Letters, 63(2):169–180.

Okuwaki, R., Kasahara, A., Yagi, Y., Hirano, S., & Fukahata, Y. (2019). Backprojection to image slip. Geophysical Journal International, 216(3), 1529-1537.

Ramachandran, P., Zoph, B., & Le, Q. V. (2017). Searching for activation functions. arXiv preprint arXiv:1710.05941.

Richardson, W. H. (1972). Bayesian-based iterative method of image restoration. JoSA, 62(1), 55-59.

Rost, S., & Thomas, C. (2002). Array seismology: Methods and applications. Reviews of Geophysics, 40(3), 1008. https://doi.org/10.1029/2000rg000100

Ruiz, J., D. Baumont, P. Bernard, and C. Berge, Modelling directivity of strong ground motion with a fractal, k-square, kinematic source model, Geophys. J. Int. 186, 226-244, 2011, doi:10.1111/j.1365-246X.2011.05000.x

Satriano, C., Dionicio, V., Miyake, H., Uchida, N., Vilotte, J. P., & Bernard, P. (2014). Structural and thermal control of seismic activity and megathrust rupture dynamics in subduction zones: Lessons from the Mw 9.0, 2011 Tohoku earthquake. Earth and Planetary Science Letters, 403, 287-298.

Schweitzer, J., Fyen, J., Mykkeltveit, S., Gibbons, S. J., Pirli, M., Kühn, D., & Kværna, T. (2012). Seismic arrays. In New manual of seismological observatory practice 2 (NMSOP-2) (pp. 1-80). Deutsches GeoForschungsZentrum GFZ.

Shunsuke Takemura, Takashi Furumura, Scattering of high-frequency P wavefield derived by dense Hi-net array observations in Japan and computer simulations of seismic wave propagations, Geophysical Journal International, Volume 193, Issue 1, April, 2013, Pages 421–436, https://doi.org/10.1093/gji/ggs127

Somerville, Paul, et al. "Characterizing crustal earthquake slip models for the prediction of strong ground motion." Seismological Research Letters 70.1 (1999): 59-80.

Spudich, P., & Frazer, L. N. (1984). Use of ray theory to calculate high-frequency radiation from earthquake sources having spatially variable rupture velocity and stress drop. Bulletin of the Seismological Society of America, 74(6), 2061-2082.

Takemura, Shunsuke & Furumura, Takashi & Maeda, Takuto. (2015). Scattering of high-frequency seismic waves caused by irregular surface topography and small-scale velocity inhomogeneity. Geophysical Journal International. 10.1093/gji/ggv038.

Vallée, M., & Satriano, C. (2014). Ten-year recurrence time between two major earthquakes affecting the same fault segment. Geophysical Research Letters, 41(7), 2312-2318.

Vallée, M., Landès, M., Shapiro, N. M., and Klinger, Y. (2008). The 14 November 2001 Kokoxili (Tibet) earthquake: High-frequency seismic radiation originating from the transitions between sub-rayleigh and supershear rupture velocity regimes. Journal of Geophysical Research: Solid Earth, 113(B7).

Walker, K. T. and Shearer, P. M. (2009). Illuminating the near-sonic rupture velocities of the intracontinental Kokoxili Mw 7.8 and Denali fault Mw 7.9 strike-slip earthquakes with global P wave back projection imaging. Journal of Geophysical Research: Solid Earth, 114(B2).

Wang, D. and Mori, J. (2016). Short-period energy of the 25 April 2015 Mw 7.8 Nepal earthquake determined from back projection using four arrays in Europe, China, Japan, and Australia. Bulletin of the Seismological Society of America, 106(1):259–266.

Wang, D., Mori, J., & Uchide, T. (2012). Supershear rupture on multiple faults for the Mw 8.6 Off Northern Sumatra, Indonesia earthquake of April 11, 2012. Geophysical research letters, 39(21).

Wang, D., Takeuchi, N., Kawakatsu, H., & Mori, J. (2016). Estimating high frequency energy radiation of large earthquakes by image deconvolution back-projection. Earth and Planetary Science Letters, 449, 155-163.

Wells, D. L., & Coppersmith, K. J. (1994). New empirical relationships among magnitude, rupture length, rupture width, rupture area, and surface displacement. Bulletin of the seismological Society of America, 84(4), 974-1002.

Xu, Y., Koper, K. D., Sufri, O., Zhu, L., & Hutko, A. R. (2009). Rupture imaging of the Mw 7.9 12 May 2008 Wenchuan earthquake from back projection of teleseismic P waves. Geochemistry, Geophysics, Geosystems, 10(4).

Yao, H., Shearer, P. M., & Gerstoft, P. (2012). Subevent location and rupture imaging using iterative backprojection for the 2011 Tohoku M w 9.0 earthquake. Geophysical Journal International, 190(2), 1152-1168.

Yagi, Yuji, Atsushi Nakao, and Amato Kasahara. "Smooth and rapid slip near the Japan Trench during the 2011 Tohoku-oki earthquake revealed by a hybrid back-projection method." Earth and Planetary Science Letters 355 (2012): 94-101.

Yukitoshi Fukahata, Yuji Yagi, Luis Rivera, Theoretical relationship between back-projection imaging and classical linear inverse solutions, Geophysical Journal International, Volume 196, Issue 1, 1 January 2014, Pages 552–559, https://doi.org/10.1093/gji/ggt392

Zeng, Y., Aki, K., & Teng, T. L. (1993). Mapping of the high-frequency source radiation for the Loma Prieta earthquake, California. Journal of Geophysical Research: Solid Earth, 98(B7), 11981-11993.

Zhang, H., & Ge, Z. (2010). Tracking the rupture of the 2008 Wenchuan earthquake by using the relative back-projection method. Bulletin of the Seismological Society of America, 100(5B), 2551-2560.

Author contribution statement:

M.C. and C.S. conceived the study. M.C. performed the computations and processed the data. M.C. C.S. and P.B. interpreted and discussed the link between the BP image and the slip function. M.C., I.M. and D.T.T. conceived the computational framework of the CNN analysis. I.M. designed the CNN architecture. M.C., I.M. and D.T.T. interpreted the data and discussed the results of the CNN analysis. M.C. drafted the manuscript. All of the authors provided critical feedback on the results and discussion and helped shape the manuscript. P.B. and P.A.J. supervised the project.

Crossref Funding Data Registry:

This study was partially supported by the European Research Council under the European Union Horizon 2020 - SERA research and innovation program. Numerical computations were performed on the S-CAPAD platform, at Institut de physique du globe de Paris (IPGP), France.

Authors e-mail addresses:

McBrearty I. : imcbrear@stanford.edu

Trugman D.T. : dtrugman@jsg.utexas.edu

Satriano C. : satriano@ipgp.fr

Johnson P.A. : paj@lanl.gov

Bernard P. : bernard@ipgp.fr

Supplementary Material

The procedure suggested by W2016 transforms the BP image conventionally calculated in the time at the source in a BP image in the apparent time of the reference station. In this new reference system, the HF emissions do no longer suffer from the 'walking effect', however they are stretched or contracted along the time axis because of the directivity effect. In **Fig.S1** we show, by way of example, the comparison between the BP image of a homogeneous rupture process calculated at the EU array following the conventional approach of Ishii et al. (2005) and the BP image of the same rupture process calculated using the W2016 reference station correction. We notice that, in the reference station system, the HF radiation is stretched along the time axis. This happens because in this example the EU array is located in the anti-directive position respect to the direction of propagation of the rupture.

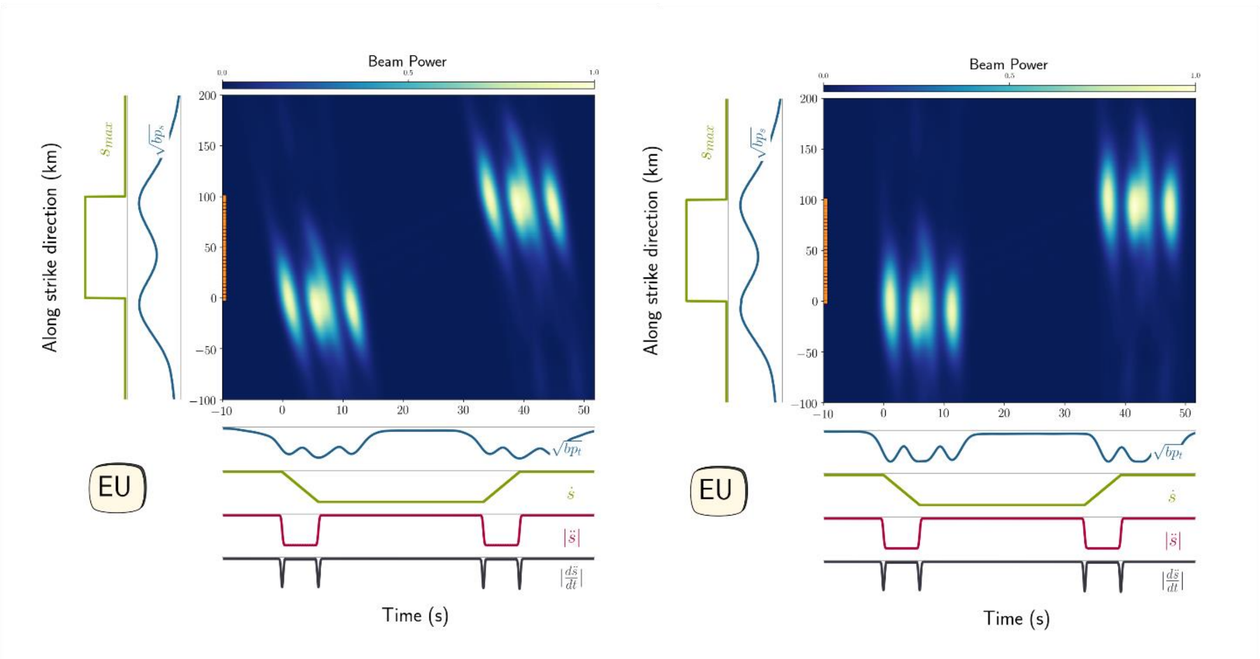

Figure S1: *HF emissions radiated by a homogeneous rupture process retrieved by BP analysis using the conventional approach (on the top) and the W2016 approach (at the bottom). Time is on the x-axis, the along strike direction is on the y-axis. The squared root of the beam power integrated in time (in blue) and the maximum value of the slip-rate function (in green) are plotted in the left subplots. The squared root of the beam power integrated in space (in blue), the slip-rate function (in green) and the absolute values of the slip-acceleration function (in red) and its time derivative (in black) are plotted in the bottom subplots. In the conventional BP analysis (BP image on the top), the HF emissions are tilted along the time axis. In the W2016 approach (BP image at the bottom), the HF emissions are stretched in time because of the directivity effect.*